

## Effect of Rotor–Stator Interaction on Impeller Performance in Centrifugal Compressors\*

K. SATO and L. HE<sup>†</sup>

*School of Engineering, University of Durham, South Road, Durham, DH1 3LE, UK*

*(Received May 1998; In final form 8 June 1998)*

**A 3-D unsteady thin-layer Navier–Stokes code has been used to calculate the flow through a centrifugal compressor stage. The validation of the code for steady flows in centrifugal compressors was conducted for the Krain’s impeller with a vaneless diffuser as a test case and the numerical results were compared with the experimental results. The predicted flow field and performance agreed well with the experimental data. An unsteady stage solution was then conducted with this impeller followed by a generic low-solidity vaned-diffuser to examine the unsteady effects on the impeller performance. The computational results showed a stabilising effect of the blade row interaction.**

*Keywords:* Centrifugal, Compressor, Impeller, Diffuser, Unsteady, CFD

### INTRODUCTION

Centrifugal compressors are characterised by their pressure generation mechanism due to the centrifugal effect. The meridional bend in addition to the circumferential bend of the impeller passages produces a highly three-dimensional flow pattern and it usually produces the well-known jet-wake flow structure at the exit of impeller. The pioneering attempt by Eckardt (1976), applying the laser anemometry for the measurement of flow through the impeller passage, clearly confirmed the generation of the wake region. More detailed flow field information was experimentally obtained by Krain (1988) with a 30° backsweep impeller. A common

feature observed in the experiments is that flows at impeller exit are highly non-uniform. If the flow field concerned is the one through the centrifugal compressor stage with vaned diffuser, this distorted flow discharged from the impeller is expected to cause a strong interaction with diffuser vanes especially when the blade rows are placed relatively close to each other. Dawes (1995) suggested that highly distorted flow emerging from the impeller did not mix-out before arriving at the diffuser vane’s entry zone as normally assumed in conventional design methods. This tendency was also recognised by Takemura and Goto (1996) with their experiment of a low specific speed pump stage, suggesting the necessity of taking into account the

\* This paper was originally presented at ISROMAC-7.

<sup>†</sup> Corresponding author. Fax.: (+44) 191-374-2550. E-mail: Li.He@durham.ac.uk.

downstream diffuser potential flow effects. They also reported that the interaction was intensified as the mass flow rate was decreased. Many researchers suggested the probability of the flow separation through the vaneless diffuser region when a centrifugal impeller was operated alone (Hathaway *et al.*, 1992; Hirsch *et al.*, 1996; Takemura and Goto, 1996). This kind of flow separation not only causes discrepancies in predicted performances between numerical simulations of isolated impellers and experiments at a design condition but also may lead the numerical simulations to be prematurely unstable at low mass-flow off design conditions.

In this paper, a 3-D unsteady thin-layer Navier–Stokes solver was used to study the downstream unsteady potential flow effect on impeller performances. The Krain’s backswept impeller was used as the test case. Firstly, for validation purposes, calculations with the impeller in isolation were carried out, and the calculated results were compared with the Krain’s experiment. On this basis, a stage calculation was conducted using the same impeller combined with low-solidity diffuser vanes to examine the blade row interaction effect on the impeller performance.

## METHOD

The code “TF3D” used in the simulations was developed by He (1996a) for multiple stage simulations of steady and unsteady flows in axial and radial turbomachinery. The flow governing equations used in this code are the 3-D unsteady compressible thin-layer Navier–Stokes equations in an absolute cylindrical co-ordinate system. The effect of turbulence was included with the Baldwin–Lomax mixing-length turbulence model. An integral form of equations is written as,

$$\begin{aligned} \frac{\partial}{\partial t} \iiint_{\Delta V} U \, dV + \iint_A [Fn_x + (G - U\varpi r)n_\theta + Hn_r] \cdot dA \\ = \iiint_{\Delta V} (S_i + S_v) \, dV \end{aligned}$$

where,

$$\begin{aligned} U &= \begin{pmatrix} \rho \\ \rho u \\ \rho vr \\ \rho w \\ \rho E \end{pmatrix}, & F &= \begin{pmatrix} \rho u \\ \rho uu + p \\ \rho uv \\ \rho uw \\ (\rho E + p)u \end{pmatrix}, \\ G &= \begin{pmatrix} \rho v \\ \rho uv \\ (\rho vv + p)r \\ \rho vw \\ (\rho E + p)v \end{pmatrix}, & H &= \begin{pmatrix} \rho w \\ \rho uw \\ \rho wvr \\ \rho ww + p \\ (\rho E + p)w \end{pmatrix}, \\ S_i &= \begin{pmatrix} 0 \\ 0 \\ 0 \\ \rho vv/r \\ 0 \end{pmatrix}. \end{aligned}$$

The mesh grids are fixed with blades. The term  $U\varpi r$  accounts for the movement of mesh grids that are associated with a rotor blade row.

The viscous effects were included in a form of body force as  $S_v$ . The viscous terms in the three momentum equations were modelled under the thin-layer assumption, so only the viscous shear stress terms in the direction tangential to the solid surfaces were included.

The equations are discretized in the finite-volume form with a cell-centred variable storage, and meshes used in the calculations are simple structured H-mesh.

The temporal integration is performed using the four stages Runge–Kutta scheme. The discretized forms of the equations are:

$$\begin{aligned} U^{n+1/4} &= U^n - \frac{1}{4} \frac{\Delta t}{\Delta A} (R_1^n - R_v^n - D^n), \\ U^{n+1/3} &= U^n - \frac{1}{3} \frac{\Delta t}{\Delta A} (R_1^{n+1/3} - R_v^n - D^n), \\ U^{n+1/2} &= U^n - \frac{1}{2} \frac{\Delta t}{\Delta A} (R_1^{n+1/2} - R_v^n - D^n), \\ U^{n+1} &= U^n - \frac{\Delta t}{\Delta A} (R_1^{n+1} - R_v^n - D^n), \end{aligned}$$

where  $R_i$  and  $R_v$  are inviscid flux and viscous terms, respectively. The numerical damping term  $D^n$  is updated once or twice through one-step time integration. The second and fourth order adaptive smoothing (Jameson, 1981) is used in all directions.

A time-consistent multiple-grid method was adopted to accelerate the convergence. While overcoming the restriction of the allowable time scale for the explicit scheme by using a complementary coarse mesh, several levels of intermediate meshes were also introduced to improve the time accuracy. The formulation of  $M$  levels time-consistent multiple-grid methods is given as (He, 1996b),

$$(U^{n+1} - U^n)_F = \Delta t_F \frac{R_F}{\Delta A_F} + \sum_{i=1}^M \Delta t_i \frac{R_i}{\Delta A_i} + \left( \Delta t - \Delta t_F - \sum_{i=1}^M \Delta t_i \right) \frac{R_c}{\Delta A_c}$$

where subscripts F, c,  $i$  denote the fine, coarse, and intermediate meshes respectively.

At an interface between two meshes fixed with the rotor and the stator, one dummy mesh cell from one blade row overlaps the mesh cell of the other blade row. For the information exchange at the interface, flow variables at the centres of the dummy cells are worked out by interpolating the flow variables in the other mesh. The information exchange is conducted at every stage of the 4-stage Runge-Kutta time integration.

At the inlet, the total pressure, total temperature and absolute flow angle are specified. At the exit, a constant static pressure is specified and other variables are extrapolated from the interior domain. The hub wall and the shroud wall are moving with the impeller while the endwall upstream and downstream of the impeller is stationary. This boundary condition assumes the impeller being shrouded in order to avoid the singularity points between the shroud and blade walls for the zero tip-clearance cases. For the calculation with tip gap, the same end wall boundary treatment was used.

## RESULTS OF SINGLE ROW CALCULATIONS

Krain's impeller combined with vaneless diffuser was chosen as a test case for the validations of the code. Series of experiments were conducted with this impeller by Krain and several published reports were available in both empirical and numerical simulation results (Krain, 1988; Hah and Krain, 1990; Hirsch *et al.*, 1996). Extensive laser anemometry measurements were performed within this impeller passage, and detailed information of flow including the jet-wake structure was obtained. This impeller has 24 full blades with 30° backward sweep, and was designed to accommodate a mass flow rate of 4.0 kg/s at a shaft speed of 22,360 rpm. The maximum achieved total pressure ratio was about 4.5, and isentropic stage efficiency was about 84%. Reduced blade loading owing to the back-sweep resulted in a comparably smooth exit velocity profile in the pitchwise direction and a high distorted profile similar to the classical jet-wake pattern was not seen with this impeller.

Initially, a structured H-mesh that consisted of  $36 \times 40 \times 95$  points (pitchwise, spanwise and meridional direction respectively) was used for steady single low calculations. Tip gap height was taken at 1.0% of blade height throughout the impeller and four grid points were allocated in the tip gap. At the same time, a comparably coarse mesh that consisted of  $26 \times 30 \times 95$  points (two points are allocated in the tip gap) was also used to assess the mesh dependency. In Krain's experiment, laser anemometry measurement was conducted at 6 measurement sections (0%, 20%, 40%, 60%, 80% and 100.4% of the chord shown in Fig. 1) in quasi-orthogonal planes to the casing wall, and these results were published in the papers of Krain (1988) and Hah and Krain (1990). In order to compare the calculation results with experiments directly, the meshes used in the calculation were fabricated so that the sections of the laser anemometry measurement corresponded to one of the quasi-orthogonal plane on the mesh.

The simulations were conducted on the Silicon Graphics Power Challenge with 12-R10000. For

the simulations with the fine mesh, approximately 10000 time-steps were required to get converged results, and it took approximately 16 h with single processor calculation. For the coarse mesh, acceptable convergence was obtained after 4000 time-steps that needed 3.3 h with single processor.

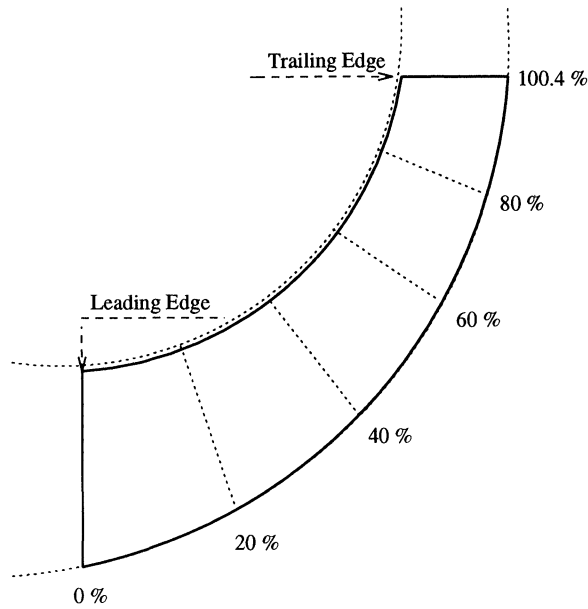


FIGURE 1 Meridional view of 6 measurement sections.

The design point of this impeller is located close to the surge line in terms of the pressure rise. Thus, the calculation was subject to a numerical surge of the impeller, which normally resulted in a failure of calculation. To attain the target mass flow rate, firstly a comparably low exit static pressure where the flow is stable was specified to avoid the surge and then the exit static pressure was carefully adjusted until the correct mass flow was attained. The calculations were conducted with both the fine and coarse meshes. The flow structure and the performance were compared at the design point. The solutions given by both fine and coarse meshes showed almost identical performance and flow structure at the design mass flow rate (Fig. 2). Other variables were also checked and it was concluded that the difference was negligible. Calculations for other conditions, presented below, were conducted with the coarse mesh. The performance map given for this impeller is shown in Fig. 3. The figures are for stagnation pressure ratios versus mass flow rate and isentropic efficiency versus mass flow. It must be pointed out that both the pressure ratio and impeller efficiency changed considerably depending on the measurement plane downstream of the impeller trailing edge since the generation of loss in the vaneless diffuser region is significant.

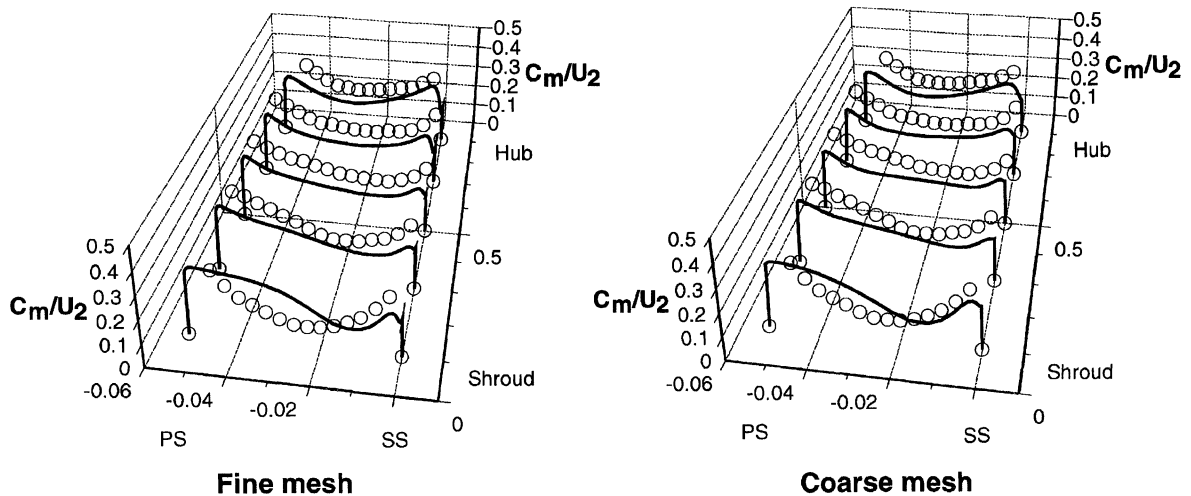


FIGURE 2 Comparison of predicted meridional velocity profiles (solid lines) at the design operating point measured at the trailing edge plane calculated with fine (left) and coarse (right) meshes with tip clearance. (Circles show the experimental results.)

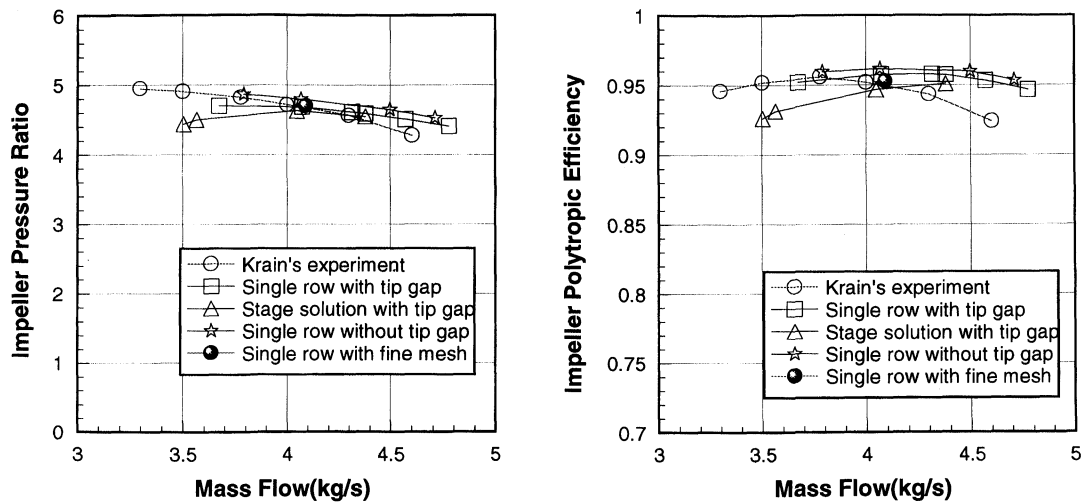


FIGURE 3 Comparisons of predicted impeller performances with experiment.

The exact measurement plane in the experiment was not known. The computational downstream plane was taken a little downstream of the impeller trailing edge where the total pressure ratio given by the simulation at design point would almost coincide with the experiment (about 13% impeller trailing edge radius away from the impeller trailing edge). The predicted pressure ratio and polytropic efficiency tended to be higher in higher mass flow rates than in the experiment. The pressure ratio without tip clearance was shown to be higher but the difference was small. Overall, the tendency was reasonably predicted.

Circumferentially averaged static pressure on the shroud wall is shown in Fig. 4 in terms of the non-dimensional meridional distance from the impeller leading edge. The predicted static pressure is in good agreement with the experimental result. Sudden change of the pressure gradient immediately after the impeller trailing edge suggests flow separation.

Figures 5 and 6 show the meridional velocity profile and the contours of the pitchwise flow angle respectively at the design point at six measurement sections. In Sections 1 and 2, the agreement between the predicted and experimental results was excellent. A low-momentum fluid region was gradually created near tip-pressure surface in Section 3, and it was reproduced in the present calculation,

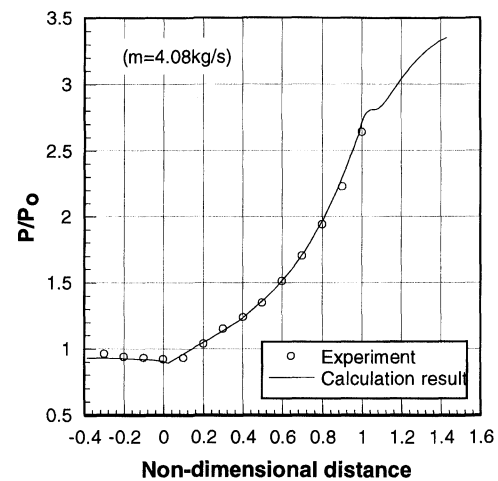


FIGURE 4 Comparison of circumferentially averaged shroud static pressure at the design operating point.

although the depth and location of the wake were slightly different. In Sections 4 and 5 this wake gradually dominated the passage. The agreement between the experiment and calculation is good apart from the region near shroud wall. The discrepancy might be attributed to the different boundary condition of the shroud wall. The shroud wall was stationary in the experiment while it was rotating at the same angular velocity with the impeller in the present calculation. This Krain's impeller was designed with the intention of lightening

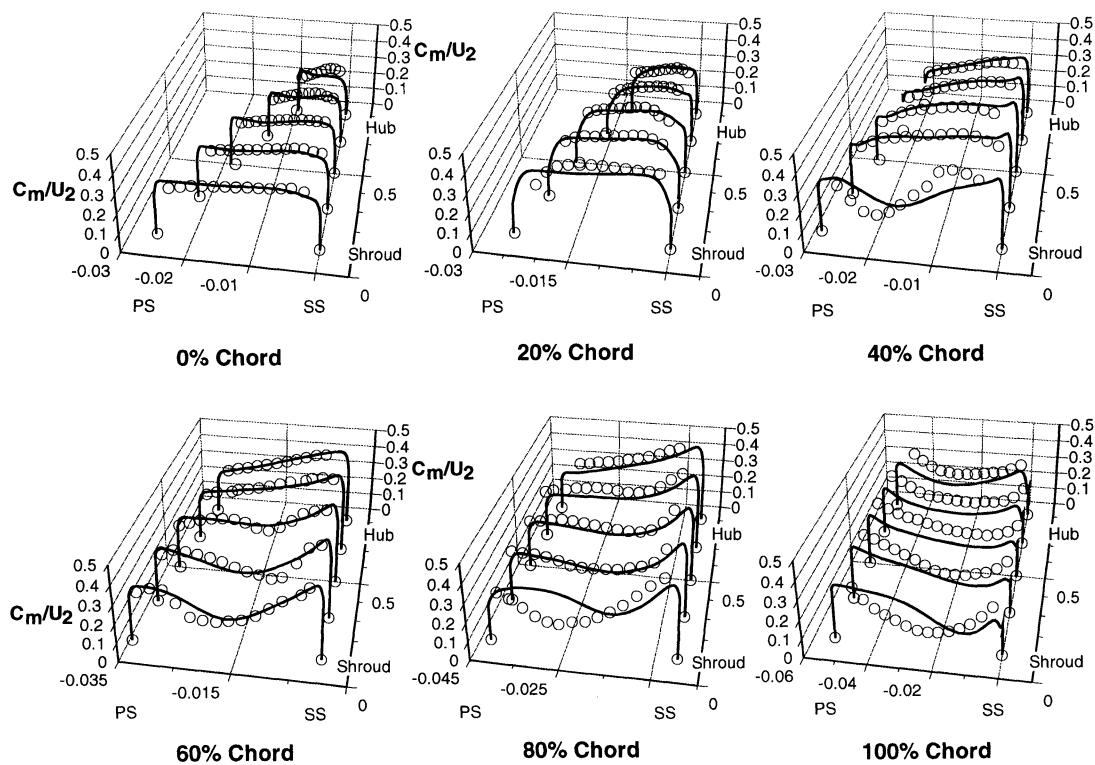


FIGURE 5 Comparisons of predicted meridional velocity with experiment (1% tip gap, design mass flow rate). Circles show the experimental data while solid lines show the predictions.

the load of the exducer part of the impeller, thus the classical jet-wake flow was not observed. Instead, a low-momentum fluid region spread over the middle passage. This nature was predicted well in Section 6. In order to estimate the influence of the tip leakage flow, calculations with no tip gap and 3% tip gap were conducted, as shown in Fig. 7. Considerable effect of the tip leakage flow was observed. The wake was always located closer to the suction side, without tip gap, indicating the convection of wake by tip leakage flow when the tip gap exists.

## RESULTS OF STAGE CALCULATIONS

During the single row impeller calculations, problems were experienced in terms of convergence at a mass flow rate below the design value. It was found that at a low mass flow rate, the flow at the trailing

edge of the impeller became separated from the casing. Further increase in pressure ratio would lead the solution to surge numerically, i.e. a continuous and irreversible reduction in mass flow, leading to a failure of the calculation. What is of interest here is how the flow separation at the impeller trailing edge is affected by an unsteady interaction with a downstream component. To assess the downstream effect on the flow in the impeller passage, an impeller-vaned diffuser stage calculation was carried out. A generic diffuser was combined with the Krain's impeller. The diffuser vanes used were low solidity vanes with straight camber lines. The incidence angle at the diffuser leading edge was set to zero at the design mass flow rate (4.0 kg/s). The radii ratio between diffuser inlet and impeller exit was 1.15 and the solidity was fixed at 0.7.

Most of the present stage calculations were carried out with a rotor/stator blade count of 1,

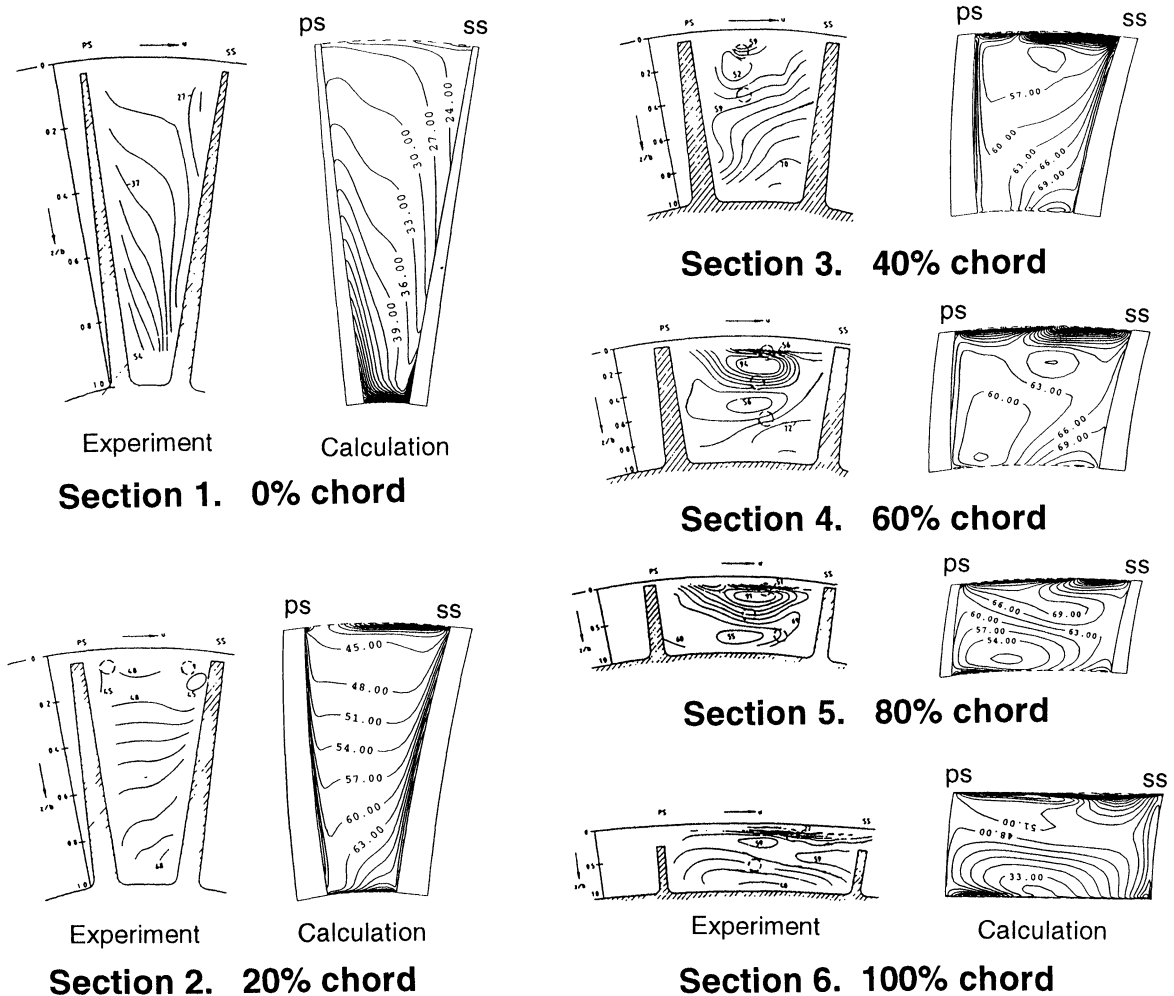


FIGURE 6 Comparisons of predicted and experimental pitchwise flow angle (1% tip gap, design mass flow rate).

i.e. one impeller passage and one diffuser passage. Some calculations were also conducted with a blade count of  $2/3$  i.e. 3 impeller passages and 2 diffuser passages. The results do not seem to show a marked difference as far as the effect on the impeller trailing edge separation is concerned. The results presented here are those for the blade count of 1. The impeller and diffuser meshes are of  $26 \times 30 \times 85$  and  $26 \times 30 \times 44$  grid points, respectively. The configuration of the mesh through the impeller passage is made exactly the same as the coarse mesh used in the steady calculations in order to eliminate the

effect due to the difference in mesh density and conduct a direct comparison. The impeller and diffuser geometry is shown in Fig. 8.

The unsteady calculation required approximately 6.5 CPU hours in a single processor SGI Power Challenge Computer for 6000 iterations corresponding to 60 blade passing periods. The time-histories of unsteady pressure near the leading edge of a diffuser blade are shown in Fig. 9. The length of the time step in the calculation was taken as one hundredth of the impeller blade-passing period seen by the diffuser blades. The stage solution was

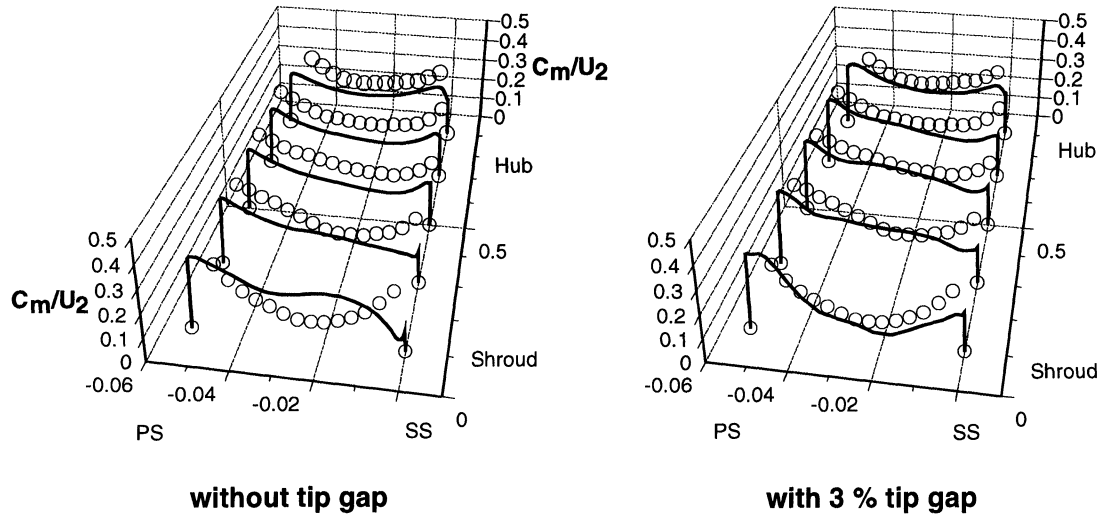


FIGURE 7 Comparison of the effect of tip gap: Predicted meridional velocity profiles at the design mass flow rate measured at the trailing edge plane without tip gap and with tip gap of 3% blade height.

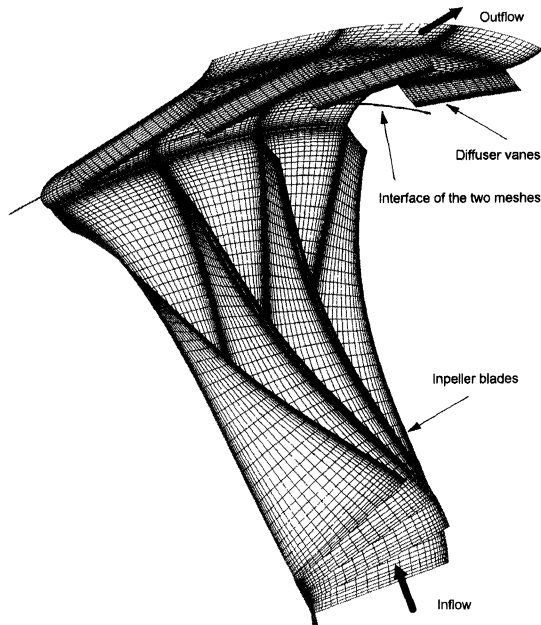


FIGURE 8 3-D view of computational meshes generated for the centrifugal impeller with diffuser vanes.

started from a 1-D initial guess, and approximately 60 periods were required to establish a periodic solution.

Figure 10 shows the instantaneous meridional velocity profiles from the stage solution. The

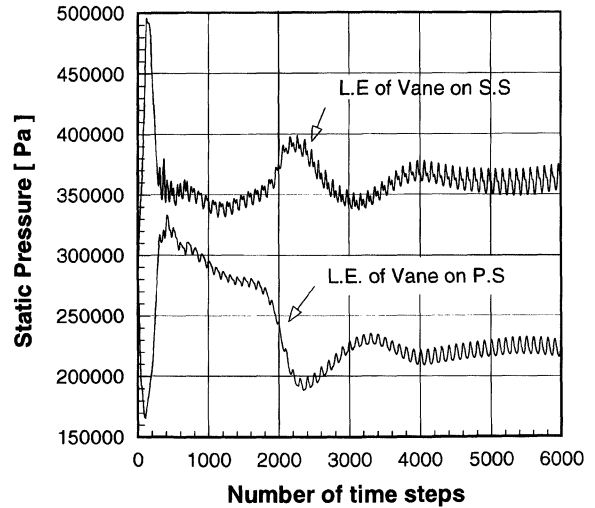


FIGURE 9 Variation of static pressure with time measured on the surfaces of diffuser vane leading edge.

relative location between the rotor and the stator is the same as that shown in Fig. 11. As far as the velocity inside the impeller is concerned, it is observed that the temporal fluctuations are small. Figure 11 shows the static pressure contours from both the single row and the stage calculations at three spanwise sections. There is a marked difference in the pressure field near the impeller trailing edge between the stage and single row results. The

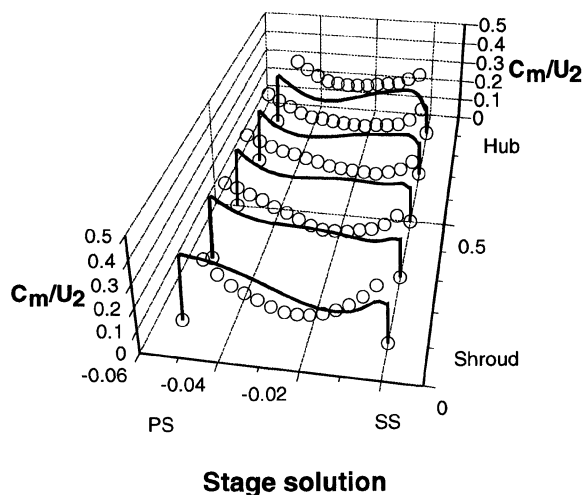


FIGURE 10 Predicted meridional velocity profile at the trailing edge of the impeller: Stage solution (1% tip gap, design mass flow rate).

single row results revealed clearly quite uniform, pitchwise, static pressure distributions at all three spanwise sections. Along the impeller flow path, the flow velocity near the tip is higher than that near the hub, resulting in a higher streamwise pressure gradient near the tip. As a result, flow separation from the casing wall was generated, which is believed to be the triggering factor of the numerical surge discussed earlier. On the other hand, the static pressure contours from the stage solution show the penetration of pressure disturbances from the diffuser vanes into the impeller passage. Thus the pressure distribution near the impeller trailing edge is both unsteady in time and non-uniform in space in the pitchwise direction. The corresponding enhanced mixing of momentum and energy exchange in time and space would affect the flow separation near the impeller trailing edge. Figure 12 shows the predicted loss contours of single row and stage solutions. Here the loss is defined as  $\exp(-S/R)$  and it is confirmed from the figures of flow vectors that the sudden growth of the loss on a wall boundary in these calculations corresponds to flow separation. For the stage solution, the contours are on a mid-pitch plane at an instantaneous time. The large scale casing separation covering the full impeller pitch observed in the single row

calculation is not visible in the stage calculation. Instead, a flow separation near the impeller trailing edge was observed on the hub surface from the stage calculation results. The separation had almost comparable scale, but it started more downstream from the trailing edge of the impeller, which is less likely to interact with the boundary layer within the impeller passage. For centrifugal compressors, the casing flow separation seems to have more severe influence on the stability since that is the part where the low-momentum fluid accumulated through the impeller passage. Consequently, this hub separation is expected to generate a less serious impact on the numerical surge, although it will have a detrimental effect on aerodynamic performances. Following the observations of these calculation results, it is speculated that the performance of the centrifugal compressor stage is very sensitive to the flow condition immediately after the impeller trailing edge.

As far as the calculated impeller characteristics are concerned, there is no noticeable difference between the single row and the stage solutions at the mass flow rates higher than the design value. The stage calculations did achieve a converged periodic solution at a lower mass flow rate compared to the single row solution, as shown in Fig. 3. Therefore the downstream unsteady interactions do seem to have a stabilising effect on the operation of the impeller blade row. Nevertheless, it is noted that although a converged solution could be achieved at a lower mass flow rate, the impeller stagnation pressure ratio and efficiency are both underpredicted in the stage case. This may well be attributed to the short-scale hub separation.

## CONCLUSIONS

The simulations of single row and stage centrifugal compressors were conducted using a 3-D thin-layer Navier-Stokes solver. The comparison of single row calculations and the Krain's experimental results for an impeller showed fair agreement. The present calculations illustrated some noticeable

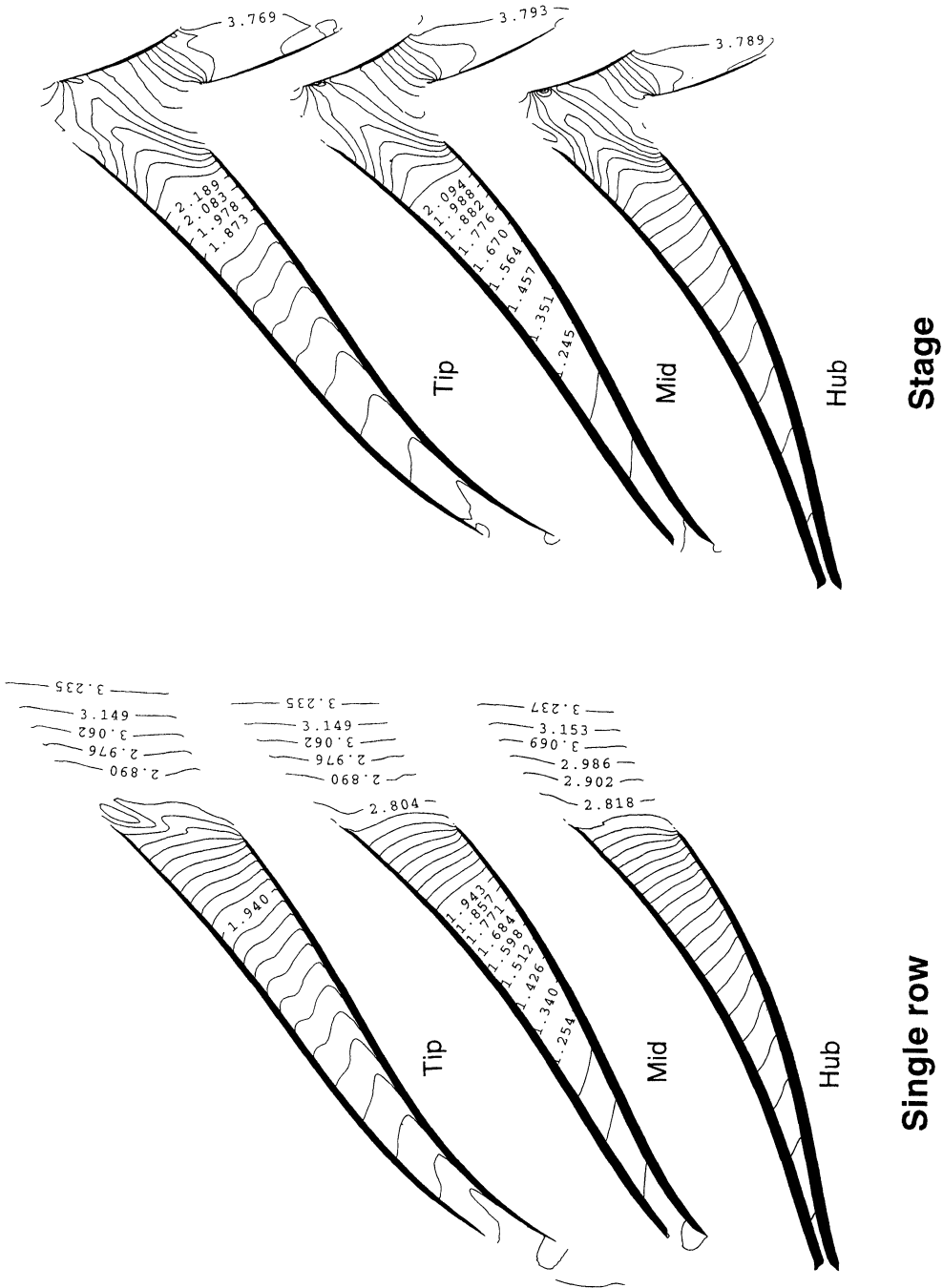


FIGURE 11 Predicted static pressure contours of single and stage solutions on three circumferential measurement plane (1% tip gap, design mass flow rate).

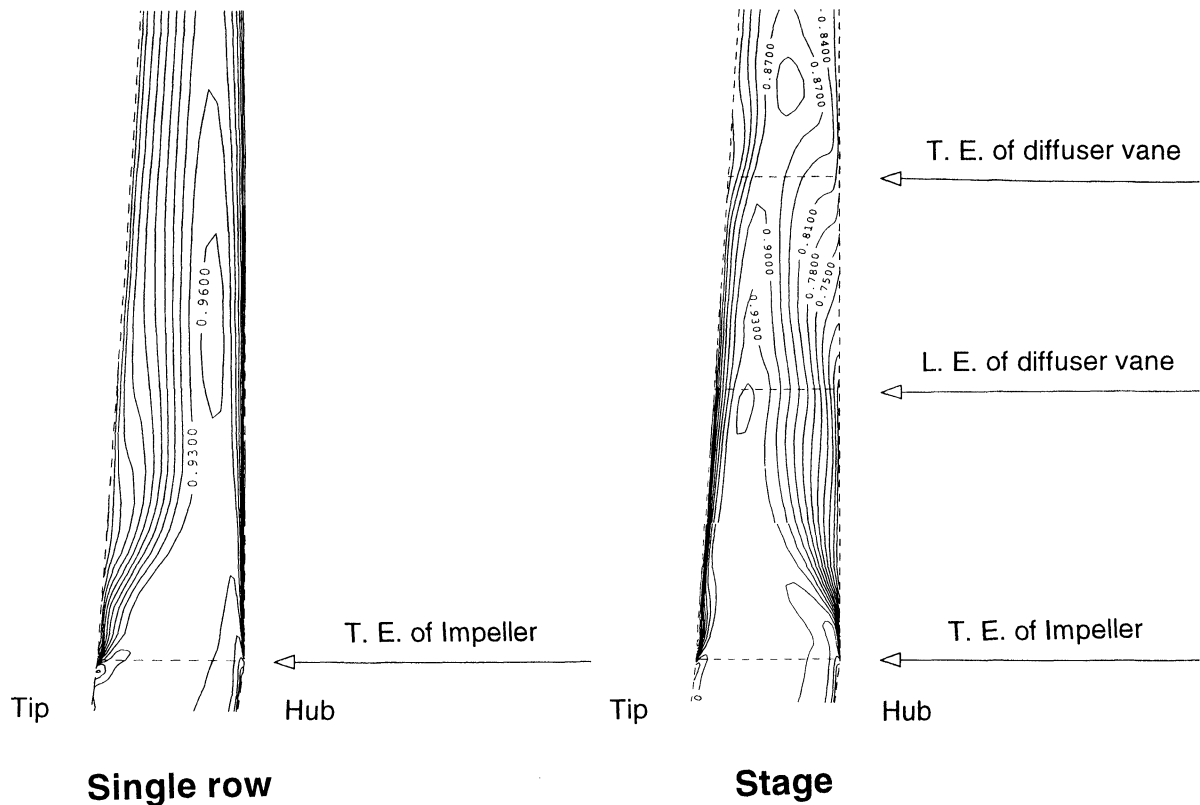


FIGURE 12 Comparison of predicted entropy contours of single and stage solutions at mid-pitch (1% tip gap, design mass flow rate).

influence of the tip leakage on the impeller flow field especially on the location of the wake, though its effect on the overall performance was not shown to be significant.

The stage calculations for Krain's impeller coupled with low-solidity diffuser vanes were carried out and the effect of the blade row interaction on the flow in the impeller passage was examined. The present computational results showed the significant influence of the downstream flow condition adjacent to the impeller trailing edge on the compressor performance. The endwall flow separations downstream of the impeller trailing edge, which triggered the instability when it interacted with the impeller flow, seemed to be delayed by the temporal and spatial static pressure non-uniformities due to the blade row interaction. The blade row

interaction effect generated a more stable flow field, compared to that from the steady single row calculations.

#### NOMENCLATURE

$A$	Area of a cell
$C_m$	Absolute meridional velocity of flow
$E$	Internal energy
$p$	Static pressure
$P_t$	Total pressure
$R$	Gas constant
$S$	Entropy
$U$	Rotational velocity of impeller
$u$	Velocity component in axial direction
$V$	Volume of a cell

$v$	Velocity component in circumferential direction
$W$	Relative velocity of flow
$w$	Velocity component in radial direction
$\rho$	Density

### Subscript

0	Stagnation condition
1	Impeller inlet
2	Impeller exit
3	Vaned diffuser inlet
4	Diffuser exit
m	Component in meridional direction
$\theta$	Component in circumferential direction

### References

- Dawes, W.N. (1995) A simulation of the unsteady interaction of a centrifugal impeller with its vaned diffuser: Flow analysis, *ASME Journal of Turbomachinery*, **117**, 213–222.
- Eckardt, D. (1976) Detailed flow investigations within a high-speed centrifugal compressor impeller, *ASME Journal of Fluids Engineering*, **98**, 390–402.
- Hah, C. and Krain, H. (1990) Secondary flows and vortex motion in a high-efficiency backswept impeller at design and off-design conditions, *ASME Journal of Turbomachinery*, **112**, 7–13.
- Hathaway, M.D., Wood, J.R. and Wasserbauer, C.A. (1992) NASA low-speed centrifugal compressor for three-dimensional viscous code assessment and fundamental flow physics research, *ASME Journal of Turbomachinery*, **114**, 295–303.
- Hirsch, C.H., Kang, S. and Pointel, G. (1996) A numerically supported investigation of the 3D flow in centrifugal impellers, Part 1: Validation base, ASME Paper No. 96-GT-151.
- He, L. (1996a) TF3D: A program to calculate turbomachinery flow in 3-dimensions, University of Durham, UK.
- He, L. (1996b) Time-marching calculations of unsteady flows, blade row interaction and flutter, VKI Lecture Series, *Unsteady Flows in Turbomachines*.
- Jameson, A., Schmidt, W. and Turkel, E. (1981) Numerical simulations of the euler equations by finite volume methods using Runge–Kutta time-stepping scheme, AIAA Paper No. 81-1259.
- Krain, H. (1988) Swirling impeller flow, *ASME Journal of Turbomachinery*, **110**, 122–128.
- Takemura, T. and Goto, A. (1996) Experimental and numerical study of three-dimensional flows in a mixed-flow pump stage, *ASME Journal of Turbomachinery*, **118**, 552–561.



# Hindawi

Submit your manuscripts at  
<http://www.hindawi.com>

